NANO LETTERS

pubs.acs.org/NanoLett
Letter

Probing the Anisotropic Fermi Surface in Tetralayer Graphene via Transverse Magnetic Focusing

Illias Klanurak, Kenji Watanabe, Takashi Taniguchi, Sojiphong Chatraphorn, and Thiti Taychatanapat*

Cite This: *Nano Lett.* 2024, 24, 6330−6336

ABSTRACT: Bernal-stacked tetralayer graphene (4LG) exhibits intriguing low-energy properties, featuring two massive sub-bands and showcasing diverse features of topologically distinct, anisotropic Fermi surfaces, including Lifshitz transitions and trigonal warping. Here, we study the influence of the band structure on electron dynamics within 4LG using transverse magnetic focusing. Our analysis reveals two distinct focusing peaks corresponding to the two sub-bands. Furthermore, we uncover a pronounced dependence of the focusing spectra on crystal orientations, indicative of an anisotropic Fermi surface. Utilizing the semiclassical model, we attribute this orientation-dependent behavior to the trigonal warping of the band structure. This phenomenon leads to variations in electron trajectories based on crystal orientation. Our findings not only enhance our understanding of the dynamics of electrons in 4LG but also offer a promising method for probing anisotropic Fermi surfaces in other materials.

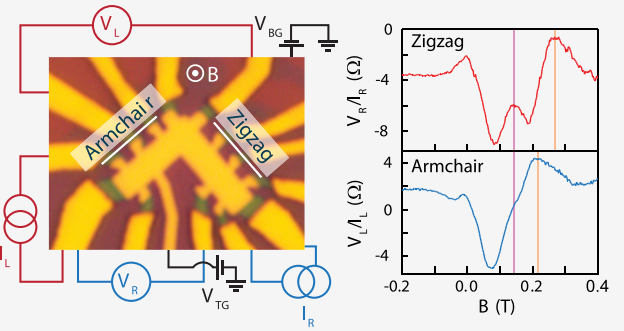

KEYWORDS: *tetralayer graphene, trigonal warping, transverse magnetic focusing, anisotropic Fermi surface*

The distinct electronic properties of multilayer graphene, in contrast to monolayer graphene, are shaped by unique features.[1−4] Trigonal warping (TW) plays a pivotal role in this differentiation, inducing a distortion of the circular Fermi surface near K and K' points in the graphene Brillouin zone due to interlayer interactions.[5] This effect introduces a discrete 3-fold rotational symmetry, breaking the continuous rotational symmetry of the Fermi surface and causing anisotropy in the low-energy band structure.[5] Numerous studies have emphasized the significance of TW, associating it with diverse phenomena such as correlated phases in bilayer graphene,[6] emergent Dirac gullies,[7] Landau level hybridization in trilayer graphene,[8] Lifshitz transitions in Bernal-stacked tetralayer graphene (4LG),[9] and topological phase transitions in twisted double bilayer graphene.[10] Recognizing the importance of the TW effect is crucial for anticipating the transport characteristics of materials

Although scanning tunneling microscopy has facilitated quasi-direct observation of the TW effect in graphene,[11] its elucidation in transport experiments remains challenging. Prior methods, including ballistic transport in bilayer graphene with superimposed antidot arrays[12] and quantum point contacts,[13] have been employed. However, these approaches could introduce inhomogeneity that can mask the intrinsic transport characteristics of bilayer graphene.[14] In our study, we leverage transverse magnetic focusing (TMF) on 4LG to investigate the low-energy anisotropic band structure associated with TW. By applying a transverse magnetic field to guide electron trajectories, TMF enables us to derive insights into the electronic properties of materials.[15−23]

The advantage of using 4LG in this study lies in its band structure, which hosts charge carriers with two distinct effective masses.[24,25] We denote the inner and outer electron (hole) bands as α_{in} (β_{in}) and α_{out} (β_{out}), respectively, as illustrated in Figure 1a. The band structure of 4LG is parametrized by the Slonczewski−Weiss−McClure (SWMcC) parameters of graphite[5] (γ_0−γ_5 and δ). Notably, the interlayer hopping parameter between nondimer sites, γ_3, is identified as a key contributor to the TW effect in multilayer graphene.[5]

The influence of γ_3 on each band at specific Fermi energies E_F can be visualized by the shape of Fermi surfaces, as shown in Figure 1b. For energy $|\epsilon(\mathbf{k})| > 8$ meV, the Fermi surfaces at each K point consist of two pockets, with those from α_{out} and β_{out} bands exhibiting more distortion than those of α_{in} and β_{in} bands. We propose that the distinct degrees of TW between the inner and outer bands can be discerned through ballistic magnetotransport measurements utilizing the TMF technique.

In TMF technique, we inject charge carriers into a two-dimensional electron gas subjected to a small perpendicular

Received: March 6, 2024
Revised: May 4, 2024
Accepted: May 8, 2024
Published: May 9, 2024

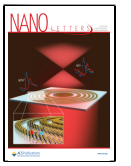

https://doi.org/10.1021/acs.nanolett.4c01133
Nano Lett. 2024, 24, 6330−6336

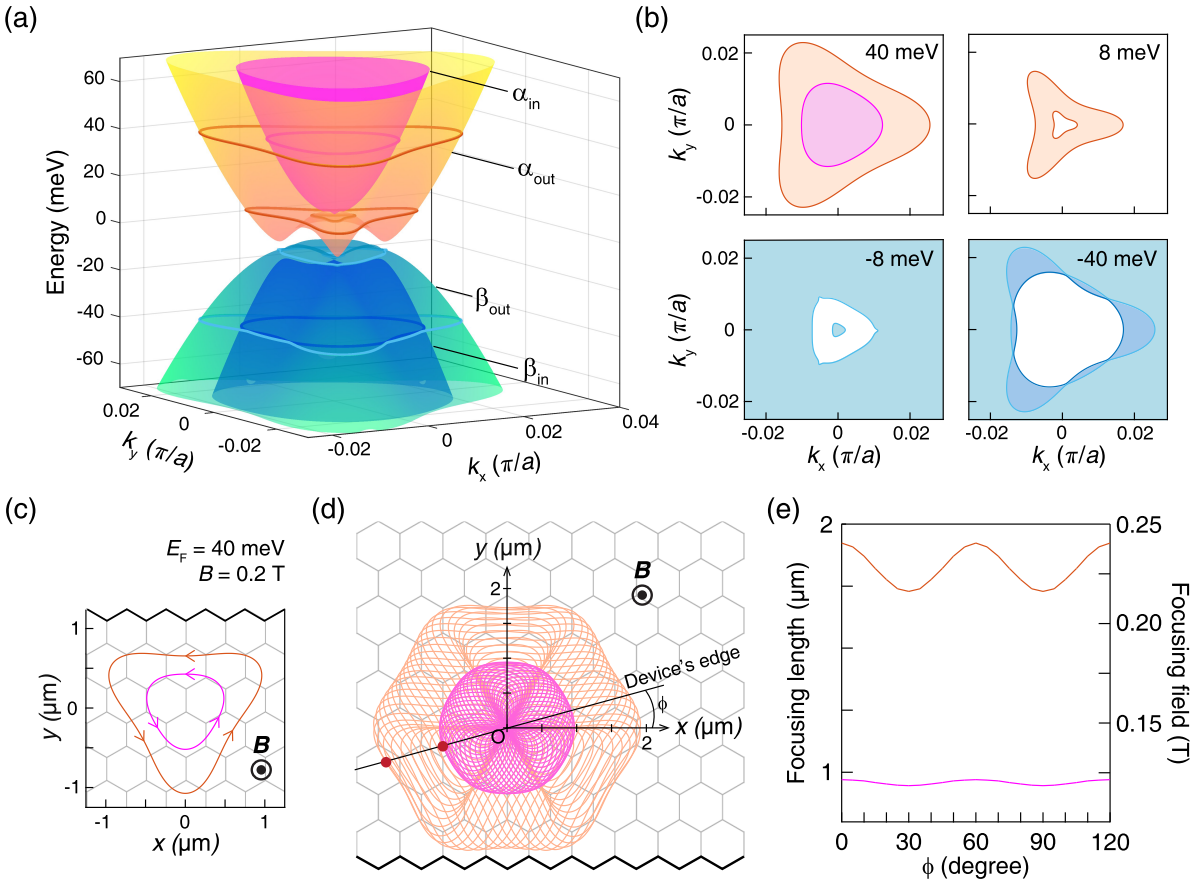

Figure 1. (a) Electronic band structure of 4LG. The inner and outer conduction bands are labeled by α_{in} and α_{out}, while the inner and outer valence bands are labeled by β_{in} and β_{out}. (b) Fermi surfaces of 4LG at 4 different Fermi energies. The shading indicates filled states for each band. (c) Electron trajectories in real space at E_F = 40 meV and magnetic field of 0.2 T. The pink and orange trajectories corresponds to electrons from α_{in} and α_{out} bands, respectively. (d) Simulated trajectories of electrons injected through point O in all directions under the same conditions as in (c). The angle ϕ measures the orientation of the device's edge relative to the zigzag edge of 4LG. The red dots indicate the focusing points at which the caustic lines intersect the device's edge. (e) Focusing length at 0.2 T and focusing field for focusing length of 1.6 μm as a function of ϕ for electron trajectories in (d).

magnetic field B. Employing the semiclassical framework,[26] the trajectories of charge carriers are dictated by the energy dispersion $\epsilon(\mathbf{k})$ at E_F. The evolution of position $\mathbf{r}$ and momentum $\hbar\mathbf{k}$ for the carriers is governed by the semiclassical equation:

$$\dot{\mathbf{r}} = \frac{1}{\hbar}\frac{d\epsilon}{d\mathbf{k}}, \qquad \hbar\dot{\mathbf{k}} = -e\dot{\mathbf{r}} \times B\hat{z}$$

where $\hbar$ is the reduced Planck constant and e is the elementary charge. In essence, the real-space trajectory of charge carriers mirrors the shape of their Fermi surfaces but is scaled by $\hbar/eB$ and rotated by 90°. As depicted in Figure 1c, electron trajectories in real space at E_F = 40 meV under B = 0.2 T are illustrated, with the x-axis aligned with the zigzag edge of 4LG. Electrons within each pocket trace closed orbits with their direction determined by the Lorentz force. Notably, electrons from the α_{in} pocket (pink path) exhibit smaller orbits in real space compared to those in the α_{out} pocket (orange path) due to the smaller size of their Fermi surface.

In Figure 1d, we depict the trajectories of electrons emanating from a point O in various directions, all under identical energy and magnetic field conditions as those shown in Figure 1c. This illustration captures how each set of trajectories within a band collectively evolves into a caustic, a zone characterized by a significantly high concentration of carriers. This results in a pronounced focusing pathway for these carriers. Notably, the α_{out} caustic exhibits heightened sensitivity to TW, leading to its adoption of a hexagonal shape, in contrast to the α_{in} caustic, which retains a more circular form. The caustic lines for each band converge on different focusing points along the device's edge, marked as red dots in Figure 1d.

Additionally, as a result of an anisotropic Fermi surface, we observe variations in the focusing length as a function of device orientation, denoted by ϕ, relative to the zigzag edge. This dependency is clearly demonstrated in Figure 1e for both the α_{in} and α_{out} bands. Specifically, Figure 1e reveals that the variability in focusing length with respect to ϕ is more pronounced for the α_{out} band, whereas it remains relatively stable for the α_{in} band. Notably, device orientations aligned with the zigzag edge (ϕ = 0°) and the armchair edge (ϕ = 90°) yield the maximum difference in focusing length and, consequently, focusing field, as illustrated in Figure 1e.

Therefore, to investigate the anisotropy of the Fermi surfaces in 4LG with TMF, we fabricate an L-shaped device, illustrated in Figure 2a. To ensure the maximum variation of the TMF signal, the left and right sides of the device are etched in parallel to the cleaved lines of the exfoliated 4LG flake, which is expected to exhibit either zigzag or armchair edges (see Supporting Information for details).[27,28]

https://doi.org/10.1021/acs.nanolett.4c01133
Nano Lett. 2024, 24, 6330−6336

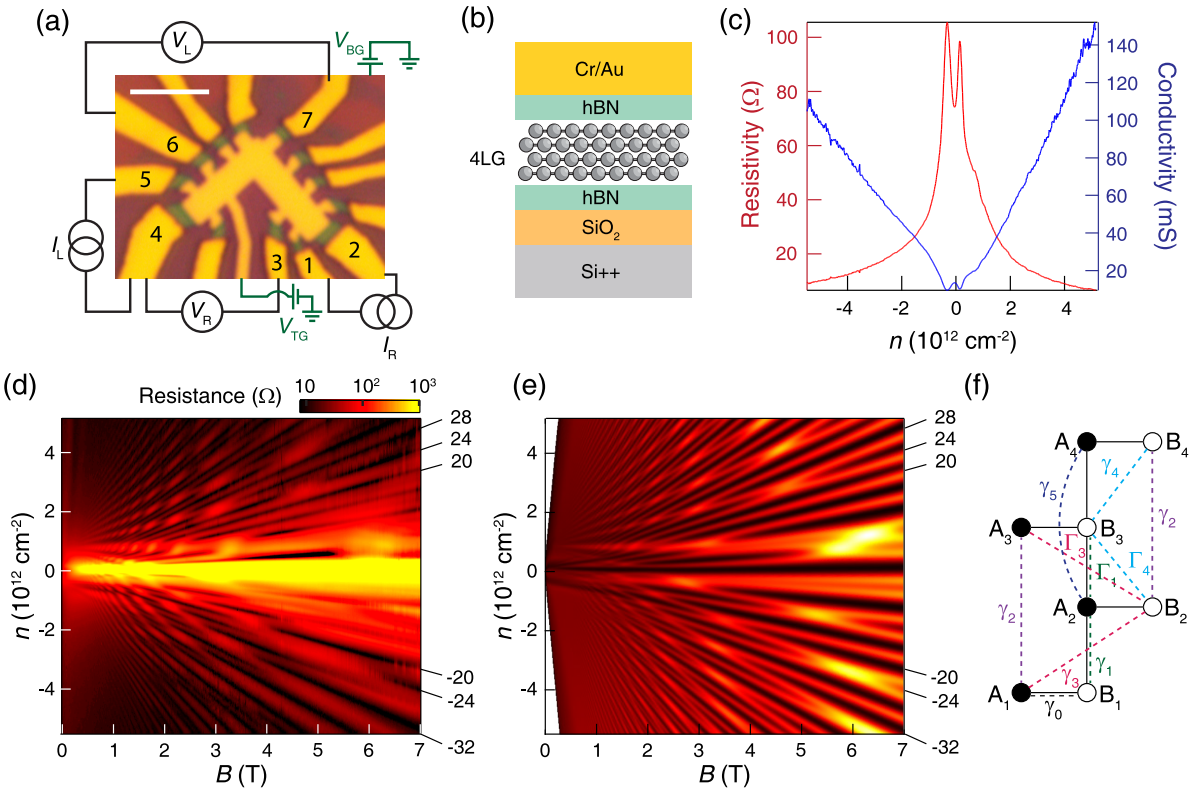

Figure 2. (a) Optical image of the 4LG device with nonlocal TMF measurement configurations, where each contact is labeled by numbers 1−7. The scale bar is 2 μm. (b) Schematic diagram of device cross section. We encapsulate a 4LG flake with top and bottom hBN flakes. Highly doped silicon and Cr/Au are used as bottom and top gates. (c) Resistivity (red line) and conductivity (blue line) as functions of n at 2.4 K from the left side of the device. (d) Longitudinal resistance as a function of B and n. (e) Calculated density of states of 4LG. The labeled numbers indicate filling factors of gap states (black lines). (f) Crystal structure of 4LG and its hopping parameters.

To explore the ballistic behavior of electrons in 4LG, we construct hBN/4LG/hBN heterostructure using the dry transfer technique,[29] depicted in Figure 2b. The heterostructure is then etched in O_2/CHF_3 plasma, while electron beam lithography along with thermal evaporation of Cr/Au are employed to define top gate and electrical contacts. Both top and back gates are utilized to independently control carrier density n and electric displacement field D. Each contact is referred to by the number labels shown in Figure 2a. All the measurements in this study are conducted at 2.4 K using the standard lock-in technique with an excitation frequency of 17 Hz. We maintain D at zero to preserve the intrinsic band structure of 4LG.

We initially evaluate the device quality by examining the longitudinal resistivity as a function of n, as illustrated in Figure 2c (see Supporting Information for details). The n value is determined from the period of Shubnikov−de Haas oscillations at a finite magnetic field. The resistivity profile reveals two distinct peaks around the charge neutrality point (CNP), along with a small shoulder at positive n, indicative of 4LG.[9] These features coincide precisely with Lifshitz transition points, which correspond to the local maxima or minima in the band structure. At large n, the conductivity demonstrates linear behavior, corresponding to field-effect mobilities of approximately 180,000 and 110,000 cm^2 V^{-1} s^{-1} for electrons and holes, respectively. These values are comparable to prior studies on ballistic transport in graphene.[12,17,30,31]

To obtain an accurate description of the band structure, we utilize Landau level (LL) crossings to determine the values of the SWMcC parameters.[32] In Figure 2d, the longitudinal resistance between contacts 5 and 6 is presented as a function of B and n. The LL crossings manifest as bright color spots in Figure 2d. By comparing the LL crossings in the simulated density of states (Figure 2e) with experimental data, we achieve excellent agreement using the SWMcC parameters reported in ref 9 ($\gamma_0 = 3$, $\gamma_1 = 0.39$, $\gamma_2 = -0.02$, $\gamma_3 = 0.3$, $\gamma_4 = 0.04$, $\gamma_5 = 0.04$, $\Gamma_1 = 0.32$, $\Gamma_3 = 0.25$, $\Gamma_4 = 0.032$, and $\delta = 0.041$ eV). Additional parameters Γ_1, Γ_3, and Γ_4 are introduced to accommodate interlayer hopping between bulk layers (see Figure 2f), reflecting differences in interlayer interactions between the bulk and surfaces of 4LG.[33]

We then perform nonlocal measurement to obtain TMF spectra for both sides of the device. Figure 2a illustrates the specific measurement configurations employed. Electron injection and collection are carried out through contacts 5 (1) and 6 (3) for the left (right) side, respectively, with a distance of 1.6 μ m between the injector and collector on both sides. The resulting TMF spectra for electrons at $n = 4 \times 10^{12}$ cm^{-2}, presented in Figure 3a as a function of B, reveal two distinct peaks at positive B, as indicated by vertical lines. These peaks, denoted as B_f, correspond to the magnetic fields required to focus electrons onto the collector. Notably, lower B_f values are associated with the α_{in} band, while higher values are linked to the α_{out} band. This difference in peak values is attributed to the larger Fermi surface of the α_{out} band compared to the α_{in} band, necessitating a stronger magnetic field for electron focusing at the same distance.

Significantly, distinctions emerge in the TMF spectra between the two sides. The B_f values for α_{in} electrons remain consistent on both sides, aligning with their nearly circular

https://doi.org/10.1021/acs.nanolett.4c01133
Nano Lett. 2024, 24, 6330−6336

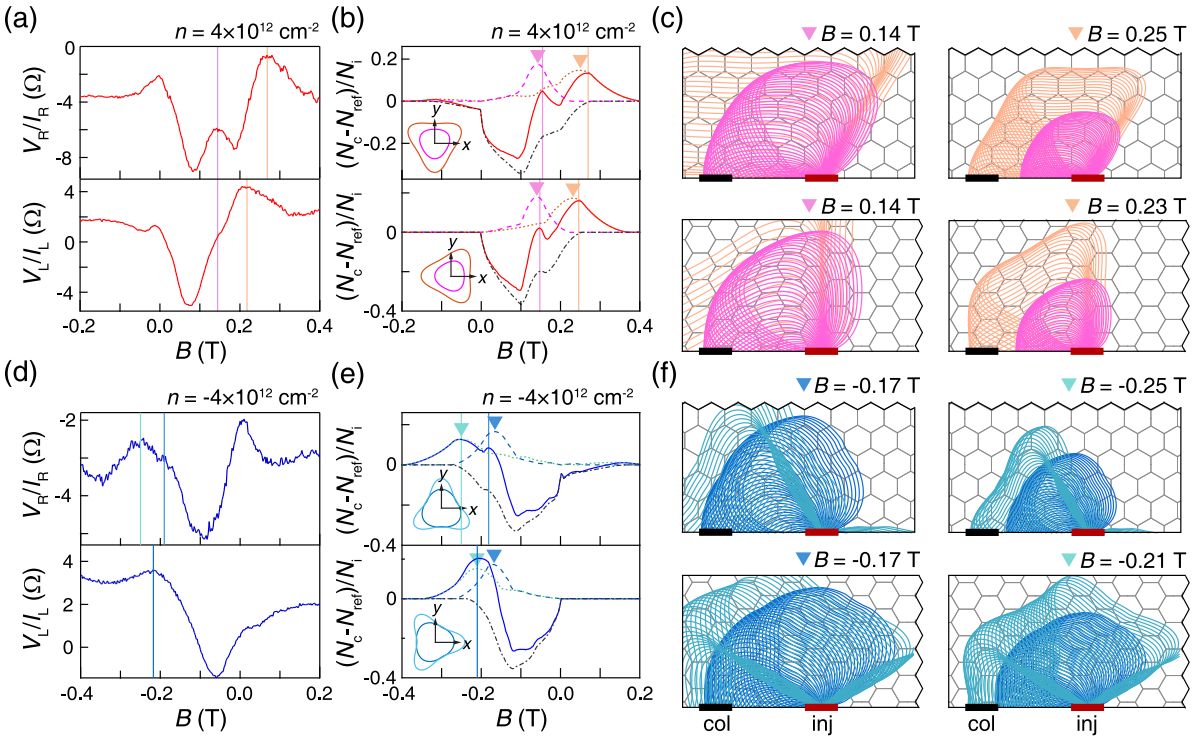

Figure 3. (a–c) Comparison of measure and simulated TMF spectra at $n = 4 \times 10^{12}$ cm^{-2}. (a) The measured TMF spectra at 2.4 K with vertical lines indicating the focusing peaks. (b) The simulated TMF spectra (solid line) alongside ratios of N_c/N_i for α_{in} and α_{out} bands (pink dashed lines and orange dotted lines, respectively). The black dashed-dotted lines represent the combined $-N_{ref}/N_i$ from both bands. (c) The simulated trajectories in real space at magnetic fields corresponding to the peak positions in (b). The red and black thick horizontal lines mark the positions of injectors and collectors, respectively. The top and bottom rows of these panels correspond to data from the right and left sides of the device, respectively. (d–e) Comparison of measured and simulated TMF spectra at $n = -4 \times 10^{12}$ cm^{-2}. (d) The measured TMF spectra at 2.4 K. (e) The simulated TMF spectra (solid line) and the ratios of N_c/N_i for β_{in} and β_{out} bands (blue dashed lines and teal dotted lines, respectively). (f) The simulated trajectories in real space.

caustic curve (see Figure 1d). Conversely, for the α_{out} band, variations in B_f values become apparent between the two sides, despite the equal distances between the injector and collector on both sides. The high mobility inherent in our device suggests that these discrepancies in B_f are not a consequence of disorder. Further, quantum Hall measurements for both sides yield identical results, confirming uniform Bernal stacking across the device (see Supporting Information for details). These observations collectively point to the anisotropic Fermi surface as the primary contributor to the observed disparity, a consequence of TW.

To confirm our assumption, we perform numerical calculations to determine TMF spectra by tracking the count of carriers reaching the collector.[19,21] The trajectories of carriers are extracted utilizing the semiclassical model from the calculated Fermi surfaces at the specified n. These Fermi surfaces are obtained from the band structure of 4LG, incorporating SWMcC parameters derived from quantum Hall data (see Supporting Information for details). The nonlocal resistance, represented as V_R/I_R, is approximated through the ratio $(N_c - N_{ref})/N_i$, where N_i is the number of injected carriers, N_c is the number of collected carriers, and N_{ref} is the number of carriers accumulated at the other reference voltage probe. We weigh the number of injected carriers in each pocket by their electronic density of states (see Supporting Information for details). In our simulation, we neglect the specular reflection of electrons at the device's edge, given the absence of higher-order peaks in our TMF data. The resulting simulation, depicted by the solid lines in Figure 3b, reveals that the best-fit values of ϕ for the right-side (RS) and left-side (LS) contacts are 0° (zigzag edge) and 90° (armchair edge), respectively. These values align with the device's design, expected to correspond to the zigzag or armchair edges of 4LG. The pink dashed lines and orange dotted lines in Figure 3b illustrate the ratio N_c/N_i for electrons from the α_{in} and α_{out} bands, respectively. Additionally, the black dashed and dotted line represents the combined ratio $-N_{ref}/N_i$ from both bands which provides a negative background in our TMF spectra.

To elucidate the physical significance of each peak, we compute the trajectories of the ensemble of injected electrons at each B_f, represented by pink (for α_{in}) and orange (for α_{out}) triangles in Figure 3b. The outcomes are presented in Figure 3c, where zigzag lines denote the orientation of the zigzag edge of 4LG. The simulation unveils that B_f for each band aligns with the magnetic field strength that focuses the maximum number of electrons onto the collector, as depicted by the caustic in Figure 3c. Moreover, it highlights that the peak positions for α_{in} electrons remain consistent for both sides, while the α_{out} peak for the LS contacts shifts toward lower B compared to the RS contacts. This behavior is attributed to the more pronounced TW effect experienced by the α_{out} electrons in contrast to the α_{in} electrons, evident from the Fermi surfaces.

While most peak positions in the simulation generally exhibit excellent alignment with the experimental data, a noticeable discrepancy arises in the actual TMF data for the left side of the device. Here, the peak corresponding to the α_{in} band manifests as a subtle shoulder rather than a distinct peak,

https://doi.org/10.1021/acs.nanolett.4c01133
Nano Lett. 2024, 24, 6330–6336

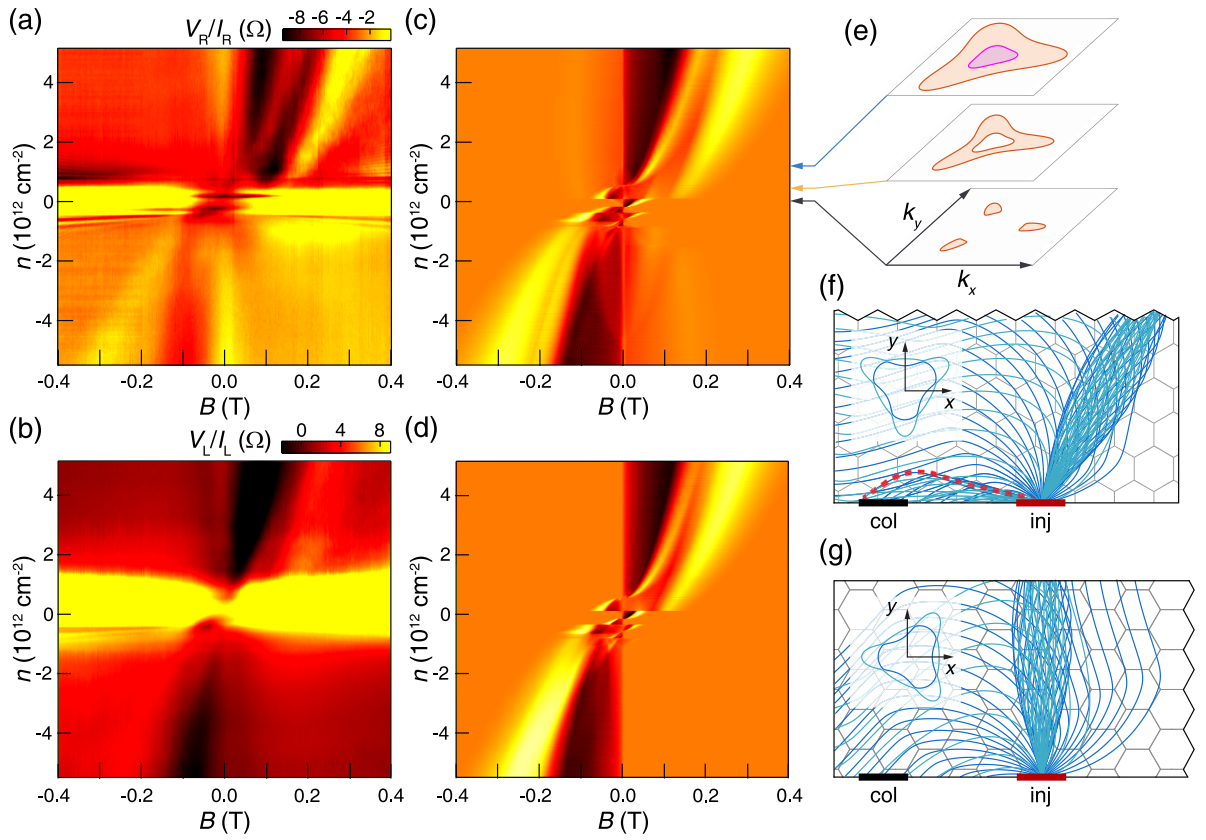

Figure 4. (a, b) Experimental TMF spectra at 2.4 K for RS and LS contacts, respectively. (c, d) Numerical simulation of the TMF data for RS and LS contacts. (e) Fermi surfaces at densities 1.2×10^{12} (blue), 4.5×10^{11} (yellow), and 1.0×10^{11} cm^{-2} (black). (f, g) Simulated trajectories of holes at $n = -2 \times 10^{12}$ cm^{-2} and $B = -0.05$ T for RS and LS contacts. The red dashed line in (f) shows a caustic. The inset shows real-space trajectories of holes in each condition.

in contrast to the simulation results (Figure 3a,b). In addition, the focusing field for the α_{out} band appears smaller than in simulation. This disparity is likely rooted in the inherent simplicity of the model employed for calculating trajectories and background signal. To enhance the precision of our analysis, more advanced methodologies, such as the Landauer−Büttiker scattering theory,[34,35] could be employed to offer a more accurate portrayal of the experimental observations. Moreover, considering the charge accumulation at boundaries resulting from graphene's finite size, which modifies carrier trajectories and impacts the focusing field, can enhance accuracy of the simulation.[17,36] However, pursuing such refinements extends beyond the scope of the present paper.

Next, we analyze the TMF spectra for holes at $n = -4 \times 10^{12}$ cm^{-2} utilizing the identical measurement configurations employed for electrons. The resulting spectra are illustrated in Figure 3d. Notably, the focusing peaks for holes manifest at negative values of B, aligning with expectations as holes possess opposite charges to electrons. Consequently, they necessitate the opposite sign of B to guide them toward the collectors. Similar to the electron regime, the spectra for the RS and LS contacts exhibit distinct characteristics. The RS spectrum features a prominent peak at $B = -0.25$ T, accompanied by a small shoulder peak around −0.18 T, consistent with the presence of two Fermi surfaces. In contrast, the LS spectrum displays a singular, broad peak at −0.21 T.

To understand the experimental data, we simulate the TMF spectra of holes as shown in Figure 3e. The simulation provides insights into the features observed in the experimental TMF spectra. Specifically, the small shoulder at −0.18 T in the RS spectrum is attributed to the focusing of β_{in} holes onto the collector, as evidenced by the trajectory simulation in Figure 3f. Meanwhile, the more pronounced peak is linked to the focusing of β_{out} holes. In the case of the LS spectrum, the simulation reveals that the focusing fields for β_{in} and β_{out} are closely matched (Figure 3e, bottom), causing the two peaks to fully merge into a single peak, consistent with our experimental data. The primary contributing factor to the broadening of the focusing peaks in our device stems from the finite width of the injector and collector, approximately 500 nm, leading to poorly resolved focusing peaks. This observation underscores the importance of considering spatial constraints in the design and interpretation of TMF spectra in nanoscale devices.

We further investigate the density dependence of TMF spectra. Figure 4a,b shows the RS and LS TMF spectra as a function of B and n. The focusing peaks are represented as bright curved ridges along diagonal in the plot. At high carrier density ($|n| > 1 \times 10^{12}$ cm^{-2}), the TMF spectra exhibit behavior consistent with those presented in Figure 3. The RS spectra manifest two distinct peaks, whereas the LS spectra display poor resolution due to the smaller difference in B_f between the two Fermi surfaces. As n decreases, B_f for each pocket also decreases. This behavior arises from the shrinking Fermi surfaces at lower carrier densities, resulting in a smaller cyclotron radius of carriers. The n-dependent TMF spectra for both sides at high density align well with the simulation, as demonstrated in Figure 4c,d. This agreement further under-

https://doi.org/10.1021/acs.nanolett.4c01133
Nano Lett. 2024, 24, 6330−6336

scores the robustness and reliability of our experimental observations and simulations across varying carrier densities.

As the electron density reduces below approximately 1×10^{12} cm^{-2}, the inner peak associated with the α_{in} band disappears (Figure 4a), in agreement with our simulation, depicted in Figure 4c. The vanishing of this inner peak results from the Fermi level dropping below the bottom edge of the α_{in} band. At these lower densities, only electrons from the α_{out} band contribute, resulting in a Fermi surface that includes both electron and hole orbits, as shown in Figure 4e (highlighted in yellow). Our simulation reveals the coexistence of electron and hole orbits within a certain density range, leading to the appearance of peaks at both positive and negative B values. As n approaches zero, the simulation shows a pronounced shift in the focusing field of the outer peak, indicative of a Lifshitz transition. This transition marks a topological transformation of the Fermi surface from a singular to three distinct smaller electron pockets (Figure 4e, black). However, in our experimental data, this Lifshitz transition is not directly observable as it occurs at densities akin to disorder-induced density fluctuations (the horizontal ridge in Figure 4a).

The simulation further unveils an additional focusing peak, as a small shoulder in the RS data near $B = -0.05$ T and $n = -2 \times 10^{12}$ cm^{-2} (Figure 4a). This supplementary peak, elucidated by the simulation, emerges due to the specific injection direction of holes in a device oriented along the zigzag direction. Figure 4f illustrates this phenomenon, where a new caustic generates a focusing path onto the collector. Notably, this extra peak is absent in the LS data corresponding to the armchair orientation. The simulation of carrier trajectories in Figure 4g aligns with this observation, as the caustic does not direct carriers toward the collector in this particular configuration. These findings underscore the orientation-dependent nuances in the TMF behavior of anisotropic Fermi surfaces.

In summary, we employed TMF to investigate the anisotropic Fermi surface in 4LG. Our findings reveal that TMF spectra distinctly vary with crystal orientations, a critical observation that underscores the sensitivity of TMF in detecting subtle electronic structure changes linked to TW effects. This variation in TMF spectra not only deepens the understanding of anisotropic properties in 4LG but also illustrates TMF's potential in elucidating the complex relationship between crystal orientation and anisotropic electronic properties in multilayer graphene. These insights have broader implications for materials with anisotropic Fermi surfaces, expanding the scope of TMF applications in material science research.

■ ASSOCIATED CONTENT

Supporting Information

The Supporting Information is available free of charge at https://pubs.acs.org/doi/10.1021/acs.nanolett.4c01133.

Device fabrication, local transport measurements, band structure calculation, TMF spectra simulation, images of individual top and bottom hBN and 4LG, flakes, four-probe longitudinal resistance, resistivity, and conductivity data, Fermi surface, trajectory of electrons in real space, and simulated trajectories of electrons (PDF)

■ AUTHOR INFORMATION

Corresponding Author

Thiti Taychatanapat − *Department of Physics, Faculty of Science, Chulalongkorn University, Bangkok 10330, Thailand;* orcid.org/0000-0002-2472-9758; Email: thiti.t@chula.ac.th

Authors

Illias Klanurak − *Department of Physics, Faculty of Science, Chulalongkorn University, Bangkok 10330, Thailand;* orcid.org/0000-0002-9309-9307

Kenji Watanabe − *Research Center for Electronic and Optical Materials, National Institute for Materials Science, Tsukuba 305-0044, Japan;* orcid.org/0000-0003-3701-8119

Takashi Taniguchi − *Research Center for Materials Nanoarchitectonics, National Institute for Materials Science, Tsukuba 305-0044, Japan;* orcid.org/0000-0002-1467-3105

Sojiphong Chatraphorn − *Department of Physics, Faculty of Science, Chulalongkorn University, Bangkok 10330, Thailand*

Complete contact information is available at: https://pubs.acs.org/10.1021/acs.nanolett.4c01133

Notes

The authors declare no competing financial interest.

■ ACKNOWLEDGMENTS

This research has been primarily supported by the NSRF via the Program Management Unit for Human Resources & Institutional Development, Research and Innovation (grant no. B05F640152), National Research Council of Thailand (NRCT) and Chulalongkorn University (grant no. N42A650266), and the Thailand Toray Science Foundation (TTSF). K.W. and T. Taniguchi acknowledge support from the JSPS KAKENHI (grant nos. 20H00354 and 23H02052) and World Premier International Research Center Initiative (WPI), MEXT, Japan.

■ REFERENCES

(1) McCann, E.; Koshino, M. The electronic properties of bilayer graphene. *Rep. Prog. Phys.* **2013**, *76*, 056503.

(2) Craciun, M. F.; Russo, S.; Yamamoto, M.; Oostinga, J. B.; Morpurgo, A. F.; Tarucha, S. Trilayer graphene is a semimetal with a gate-tunable band overlap. *Nat. Nanotechnol.* **2009**, *4*, 383−388.

(3) Datta, B.; Dey, S.; Samanta, A.; Agarwal, H.; Borah, A.; Watanabe, K.; Taniguchi, T.; Sensarma, R.; Deshmukh, M. M. Strong electronic interaction and multiple quantum Hall ferromagnetic phases in trilayer graphene. *Nat. Commun.* **2017**, *8*, 14518.

(4) Hirahara, T.; Ebisuoka, R.; Oka, T.; Nakasuga, T.; Tajima, S.; Watanabe, K.; Taniguchi, T.; Yagi, R. Multilayer graphene shows intrinsic resistance peaks in the carrier density dependence. *Sci. Rep.* **2018**, *8*, 13992.

(5) Charlier, J.-C.; Gonze, X.; Michenaud, J.-P. First-principles study of the electronic properties of graphite. *Phys. Rev. B* **1991**, *43*, 4579.

(6) Seiler, A. M.; Geisenhof, F. R.; Winterer, F.; Watanabe, K.; Taniguchi, T.; Xu, T.; Zhang, F.; Weitz, R. T. Quantum cascade of correlated phases in trigonally warped bilayer graphene. *Nature* **2022**, *608*, 298−302.

(7) Zibrov, A. A.; Rao, P.; Kometter, C.; Spanton, E. M.; Li, J.; Dean, C. R.; Taniguchi, T.; Watanabe, K.; Serbyn, M.; Young, A. F. Emergent Dirac Gullies and Gully-Symmetry-Breaking Quantum Hall States in A B A Trilayer Graphene. *Phys. Rev. Lett.* **2018**, *121*, 167601.

(8) Datta, B.; Agarwal, H.; Samanta, A.; Ratnakar, A.; Watanabe, K.; Taniguchi, T.; Sensarma, R.; Deshmukh, M. M. Landau level diagram

and the continuous rotational symmetry breaking in trilayer graphene. *Phys. Rev. Lett.* **2018**, *121*, 056801.
(9) Shi, Y.; Che, S.; Zhou, K.; Ge, S.; Pi, Z.; Espiritu, T.; Taniguchi, T.; Watanabe, K.; Barlas, Y.; Lake, R.; Lau, C. N. Tunable Lifshitz transitions and multiband transport in tetralayer graphene. *Phys. Rev. Lett.* **2018**, *120*, 096802.
(10) Mohan, P.; Ghorai, U.; Sensarma, R. Trigonal warping, satellite dirac points, and multiple field tuned topological transitions in twisted double bilayer graphene. *Phys. Rev. B* **2021**, *103*, 155149.
(11) Joucken, F.; Ge, Z.; Quezada-López, E. A.; Davenport, J. L.; Watanabe, K.; Taniguchi, T.; Velasco, J., Jr Determination of the trigonal warping orientation in Bernal-stacked bilayer graphene via scanning tunneling microscopy. *Phys. Rev. B* **2020**, *101*, 161103.
(12) Oka, T.; Tajima, S.; Ebisuoka, R.; Hirahara, T.; Watanabe, K.; Taniguchi, T.; Yagi, R. Ballistic transport experiment detects Fermi surface anisotropy of graphene. *Phys. Rev. B* **2019**, *99*, 035440.
(13) Ingla-Aynés, J.; Manesco, A. L. R.; Ghiasi, T. S.; Volosheniuk, S.; Watanabe, K.; Taniguchi, T.; van der Zant, H. S. J. Specular electron focusing between gate-defined quantum point contacts in bilayer graphene. *Nano Lett.* **2023**, *23*, 5453−5459.
(14) Lee, Y. K.; Smith, J. S.; Cole, J. H. Influence of Device Geometry and Imperfections on the Interpretation of Transverse Magnetic Focusing Experiments. *Nanoscale Res. Lett.* **2022**, *17*, 31.
(15) Van Houten, H.; Beenakker, C. W. J.; Williamson, J. G.; Broekaart, M. E. I.; Van Loosdrecht, P. H. M.; Van Wees, B. J.; Mooij, J. E.; Foxon, C. T.; Harris, J. J. Coherent electron focusing with quantum point contacts in a two-dimensional electron gas. *Phys. Rev. B* **1989**, *39*, 8556.
(16) Rokhinson, L. P.; Larkina, V.; Lyanda-Geller, Y. B.; Pfeiffer, L. N.; West, K. W. Spin separation in cyclotron motion. *Phys. Rev. Lett.* **2004**, *93*, 146601.
(17) Taychatanapat, T.; Watanabe, K.; Taniguchi, T.; Jarillo-Herrero, P. Electrically tunable transverse magnetic focusing in graphene. *Nat. Phys.* **2013**, *9*, 225−229.
(18) Chen, S.; Han, Z.; Elahi, M. M.; Habib, K. M. M.; Wang, L.; Wen, B.; Gao, Y.; Taniguchi, T.; Watanabe, K.; Hone, J.; Ghosh, A. W.; Dean, C. R. Electron optics with p−n junctions in ballistic graphene. *Science* **2016**, *353*, 1522−1525.
(19) Lee, M.; Wallbank, J. R.; Gallagher, P.; Watanabe, K.; Taniguchi, T.; Fal'ko, V. I.; Goldhaber-Gordon, D. Ballistic miniband conduction in a graphene superlattice. *Science* **2016**, *353*, 1526−1529.
(20) Lo, S.-T.; Chen, C.-H.; Fan, J.-C.; Smith, L. W.; Creeth, G. L.; Chang, C.-W.; Pepper, M.; Griffiths, J. P.; Farrer, I.; Beere, H. E.; et al. Controlled spatial separation of spins and coherent dynamics in spin-orbit-coupled nanostructures. *Nat. Commun.* **2017**, *8*, 15997.
(21) Berdyugin, A. I.; Tsim, B.; Kumaravadivel, P.; Xu, S. G.; Ceferino, A.; Knothe, A.; Kumar, R. K.; Taniguchi, T.; Watanabe, K.; Geim, A. K.; et al. Minibands in twisted bilayer graphene probed by magnetic focusing. *Sci. Adv.* **2020**, *6*, eaay7838.
(22) Gupta, A.; Heremans, J. J.; Kataria, G.; Chandra, M.; Fallahi, S.; Gardner, G. C.; Manfra, M. J. Precision measurement of electron-electron scattering in GaAs/AlGaAs using transverse magnetic focusing. *Nat. Commun.* **2021**, *12*, 5048.
(23) Rao, Q.; Kang, W.-H.; Xue, H.; Ye, Z.; Feng, X.; Watanabe, K.; Taniguchi, T.; Wang, N.; Liu, M.-H.; Ki, D.-K. Ballistic transport spectroscopy of spin-orbit-coupled bands in monolayer graphene on WSe2. *Nat. Commun.* **2023**, *14*, 6124.
(24) Koshino, M.; McCann, E. Landau level spectra and the quantum Hall effect of multilayer graphene. *Phys. Rev. B* **2011**, *83*, 165443.
(25) Klanurak, I.; Watanabe, K.; Taniguchi, T.; Chatraphorn, S.; Taychatanapat, T. Magnetoconductance oscillations in electron-hole hybridization gaps and valley splittings in tetralayer graphene. *Phys. Rev. B* **2022**, *106*, L161405.
(26) Ashcroft, N. W.; Mermin, N. D. *Solid State Physics*; Cengage Learning, 2022.
(27) Neubeck, S.; You, Y. M.; Ni, Z. H.; Blake, P.; Shen, Z. X.; Geim, A. K.; Novoselov, K. S. Direct determination of the crystallographic orientation of graphene edges by atomic resolution imaging. *Appl. Phys. Lett.* **2010**, *97*, 053110.
(28) Almeida, C. M.; Carozo, V.; Prioli, R.; Achete, C. A. Identification of graphene crystallographic orientation by atomic force microscopy. *J. Appl. Phys.* **2011**, *110*, 086101.
(29) Wang, L.; Meric, I.; Huang, P. Y.; Gao, Q.; Gao, Y.; Tran, H.; Taniguchi, T.; Watanabe, K.; Campos, L. M.; Muller, D. A.; Guo, J.; Kim, P.; Hone, J.; Shepard, K. L.; Dean, C. R. One-dimensional electrical contact to a two-dimensional material. *Science* **2013**, *342*, 614−617.
(30) Mayorov, A. S.; Gorbachev, R. V.; Morozov, S. V.; Britnell, L.; Jalil, R.; Ponomarenko, L. A.; Blake, P.; Novoselov, K. S.; Watanabe, K.; Taniguchi, T.; Geim, A. K. Micrometer-scale ballistic transport in encapsulated graphene at room temperature. *Nano Lett.* **2011**, *11*, 2396−2399.
(31) Sandner, A.; Preis, T.; Schell, C.; Giudici, P.; Watanabe, K.; Taniguchi, T.; Weiss, D.; Eroms, J. Ballistic transport in graphene antidot lattices. *Nano Lett.* **2015**, *15*, 8402−8406.
(32) Taychatanapat, T.; Watanabe, K.; Taniguchi, T.; Jarillo-Herrero, P. Quantum Hall effect and Landau-level crossing of Dirac fermions in trilayer graphene. *Nat. Phys.* **2011**, *7*, 621−625.
(33) Wu, Z.; et al. Detection of interlayer interaction in few-layer graphene. *Phys. Rev. B* **2015**, *92*, 075408.
(34) Beconcini, M.; Valentini, S.; Kumar, R. K.; Auton, G. H.; Geim, A. K.; Ponomarenko, L. A.; Polini, M.; Taddei, F. Scaling approach to tight-binding transport in realistic graphene devices: The case of transverse magnetic focusing. *Phys. Rev. B* **2016**, *94*, 115441.
(35) Petrović, M. D.; Milovanović, S. P.; Peeters, F. M. Scanning gate microscopy of magnetic focusing in graphene devices: quantum versus classical simulation. *Nanotechnology* **2017**, *28*, 185202.
(36) Silvestrov, P. G.; Efetov, K. B. Charge accumulation at the boundaries of a graphene strip induced by a gate voltage: Electrostatic approach. *Phys. Rev. B* **2008**, *77*, 155436.

https://doi.org/10.1021/acs.nanolett.4c01133
Nano Lett. 2024, 24, 6330−6336